Tuning in scene-preferring cortex for mid-level visual features gives rise to selectivity across multiple levels of stimulus complexity

Shi Pui Donald Li and Michael F. Bonner

Department of Cognitive Science, Johns Hopkins University, Baltimore, MD, USA

Please address correspondence to:
Shi Pui Donald Li or Michael F. Bonner
Department of Cognitive Science
Johns Hopkins University
3400 N. Charles Street
Baltimore, MD 21218
Email: sli97@jhu.edu, mfbonner@jhu.edu

Author Contributions:	SPDL collected data, performed analyses, and wrote the manuscript. MFB supervised the project and wrote the manuscript.
Conflicts of interest:	nothing to declare
Classification:	Biological Sciences/Psychological and Cognitive Sciences
Keywords:	mid-level features, scene-selective cortex, deep neural networks, encoding models, fMRI, curvature, real-world size, landmarks
Figures:	4
Supplemental figures:	10

ABSTRACT

The scene-preferring portion of the human ventral visual stream, known as the parahippocampal place area (PPA), responds to scenes and landmark objects, which tend to be large in real-world size, fixed in location, and inanimate. However, the PPA also exhibits preferences for low-level contour statistics, including rectilinearity and cardinal orientations, that are not directly predicted by theories of scene- and landmark-selectivity. It is unknown whether these divergent findings of both low- and high-level selectivity in the PPA can be explained by a unified computational theory. To address this issue, we fit hierarchical computational models of mid-level tuning to the image-evoked fMRI responses of the PPA, and we performed a series of high-throughput experiments on these models. Our findings show that hierarchical encoding models of the PPA exhibit emergent selectivity across multiple levels of complexity, giving rise to high-level preferences along dimensions of real-world size, fixedness, and naturalness/animacy as well as low-level preferences for rectilinear shapes and cardinal orientations. These results reconcile disparate theories of PPA function in a unified model of mid-level visual representation, and they demonstrate how multifaceted selectivity profiles naturally emerge from the hierarchical computations of visual cortex and the natural statistics of images.

SIGNIFICANCE STATEMENT

Visual neuroscientists characterize cortical selectivity by identifying stimuli that drive regional responses. A perplexing finding is that many higher-order visual regions exhibit selectivity spanning multiple levels of complexity: they respond to highly complex categories, such as scenes and landmarks, but also to surprisingly simplistic features, such as specific contour orientations. Using large-scale computational analyses and human brain imaging, we show how multifaceted selectivity in scene-preferring cortex can emerge from the coding of mid-level visual features, whose complexity is neither as simple as local contours nor as complex as scenes or objects. Our work reconciles seemingly divergent findings of selectivity in scene-preferring cortex and suggests that mid-level features may be central to understanding the category-selective organization of the human visual system.

MAIN TEXT

INTRODUCTION

A central goal of visual neuroscience is to identify the stimulus properties that selectively drive the responses of neural populations in visual cortex. In high-order visual areas, responses often exhibit complex and unintuitive patterns of multifaceted selectivity for stimulus properties spanning from low-level image features to high-level conceptual attributes (1–4). Several lines of research suggest that the multifaceted selectivity profiles of higher-order visual regions cannot be reduced to a single level of explanation: neither low-level perceptual factors nor high-level conceptual factors fully account for cortical response preferences (5–9). Thus, a major challenge for visual neuroscience is to explain how such multifaceted selectivity profiles emerge from the information-processing mechanisms of visual cortex.

The parahippocampal place area (PPA) is a clear example of such multifaceted selectivity. The PPA is a scene-preferring area of the ventral visual stream that responds strongly to spatial scenes (10). A longstanding hypothesis of the PPA is that it selectively processes large scene elements, including spatial structures and objects, that can serve as navigational landmarks (11–16). This hypothesis is primarily motivated by the strong global signal modulation of the PPA in response to scenes and to objects that are large in real-world size, spatially fixed, and inanimate (13, 16). However, other work has shown that the responses of the PPA are also modulated by low-level visual features, with a specific preference for high spatial-frequency contours that form rectilinear junctions and are oriented along the cardinal axes (17–19). Low-level features can even drive the responses of the PPA when presented in minimal stimuli, such as basic geometric shapes, that do not resemble natural scenes or landmarks (18, 19).

The existence of low-level feature preferences in the PPA has been argued to be inconsistent with theories of landmark-specialization, and it has sparked a debate over the appropriate level of interpretation for PPA selectivity (2, 6, 17–19). However, several findings suggest that the response preferences of the PPA cannot be fully explained by low-level features alone. First, the PPA shows a preference for scenes even when they are matched to comparison stimuli on low-level properties (17, 20). Second, the PPA exhibits a preference for spatial scenes and large objects even in the absence of visual stimulation, when sighted subjects haptically explore miniature scenes or when blind subjects are cued to think of large objects (21, 22). Nonetheless, the low-level feature preferences of the PPA remain to be explained. Understanding how these low-level preferences square with findings of scene- and landmark-selectivity is critical for developing a complete theory of the PPA, and it may have broader implications for understanding the complex tuning functions of category-selective visual cortex more broadly.

We explored the possibility that the multifaceted selectivity profile of the PPA can be understood as an emergent property of the hierarchical computations of visual cortex and the natural statistics of scenes (6, 23). We focused specifically on the representation of mid-level visual features, which are more complex than simple oriented contours but less complex than the semantic attributes of objects (24, 25). Our hypothesis was that the feedforward computation of mid-level features is sufficient to explain several high-level selectivity findings in the PPA and that a direct consequence of these feedforward computations is the emergence of low-level biases for cardinal orientations and rectilinear shapes. This hypothesis is premised on a simple principle of computational hierarchies: that higher-level representations inherit the biases of their downstream inputs. It is known that the PPA inherits at least one type of low-level bias in the form of a retinotopic preference for the upper and peripheral visual field (26), and it has been speculated that scene areas exhibit preferences for the low-level features that are most associated with scenes and landmarks (2, 6). However, no previous studies have determined whether the multifaceted selectivity profile of the PPA naturally emerges from a feedforward computational hierarchy.

To test our hypothesis, we fit hierarchical neural network models of mid-level visual representation to the scene-evoked fMRI responses of the PPA. We then ran a series of high-throughput *in-silico* experiments on these models to characterize their selectivity to multiple properties of both natural images and simple geometric stimuli. We found that the feedforward coding of mid-level features is sufficient to predict the fMRI responses of the PPA to natural scenes and objects and to reproduce the selectivity profile of the PPA across multiple levels of complexity for tens of thousands of images, including selectivity for scenes, selectivity for objects that are large, inanimate, manmade, and spatially fixed, and selectivity for the low-level contour statistics of rectilinearity and cardinal orientations. These findings suggest that the multifaceted selectivity profile of the PPA may naturally emerge from the feedforward coding of mid-level visual features and the statistical regularities of images.

RESULTS

Encoding model of mid-level feature tuning

We used convolutional neural networks (CNNs) and fMRI data to create image-computable voxelwise encoding models of mid-level feature tuning in the PPA. CNNs are theoretical models of the core information-processing mechanisms implemented by biological neural populations, and they are the leading computational models of human visual cortex (27), including scene-selective areas (23, 28). They perform a set of biologically plausible mathematical operations, and their hierarchical, convolutional architecture is inspired by the primate visual system. CNNs take images as inputs and pass them through a hierarchy of nonlinear transformations whose final outputs support image classification (after model training). A major strength of CNNs is that they make explicit predictions about the stimulus transformations that may occur along the processing hierarchy of visual cortex. This makes CNNs ideally suited for testing theories about the computational basis of multifaceted selectivity.

We developed voxelwise computational models of mid-level feature tuning by mapping the outputs of a feedforward CNN to fMRI responses in four subjects from the BOLD5000 dataset who viewed between 2,952 and 4,916 unique natural scene images depicting real-world environments and objects (29). We used the AlexNet CNN architecture pre-trained on ImageNet (30). The first five layers of AlexNet are convolutional layers, whose units receive inputs from spatially local regions of the previous layer, like the spatial receptive field structure of visual cortex. Each unit performs a linear-nonlinear operation in which it computes a weighted linear sum of its inputs followed by a nonlinear activation function (specifically, a rectified linear threshold). The weights on the inputs for each unit define a type of feature channel, and each convolutional layer contains a set of feature channels that are replicated with the same set of weights over the entire image. Our modelling procedure involved pooling and reweighting of the CNN responses from the last convolutional layer (layer 5) to predict the image-evoked fMRI responses in the BOLD5000 dataset (Fig. 1A). We were specifically interested in characterizing feature tuning in the PPA rather than retinotopic biases. We therefore created a set of fully spatially invariant feature activations by applying global max pooling across all spatial locations for each feature channel in layer 5. The outputs of this global max pooling operation were passed to a linear regression layer that we trained to predict fMRI responses as a weighted sum of feature activations. We used regularized regression to develop sparse models of feature tuning that focus on the most informative features for each voxel. We compared cross-validated performance when using LASSO (L1 penalized), which encourages sparse models, ridge (L2 penalized), and ordinary least squares (OLS) regression. We found that LASSO outperformed both ridge and OLS regression, suggesting that our models of feature tuning benefited from the inclusion of

a regularization term that pushes a portion of the regression weights to zero (Supplementary Fig. 1).

We assessed the reliability of encoding model performance in two ways. We first used cross-validation to examine out-of-sample prediction accuracy on the BOLD5000 dataset and found that the prediction accuracy in the PPA was statistically significant (Supplementary Fig. 2A). We next performed a stringent test of how well our encoding models could generalize to new data by examining their ability to predict the average responses of the PPA in a separate fMRI dataset with different subjects and novel stimuli. We examined data from an fMRI study of object representation in which four subjects viewed images of isolated objects from 81 different categories (31). We found that our encoding models trained on the BOLD5000 dataset were highly accurate at predicting the fMRI responses of the PPA to novel stimuli in a completely different set of subjects (Fig. 1B; r=0.58, p=1e-5; see other visual ROIs in Supplementary Fig. 2B). The strong generalization performance of our encoding models suggests that they capture important aspects of the feature preferences of the PPA and, furthermore, that these feature preferences explain a substantial portion of variance in the responses of the PPA to a wide range of stimuli, including complex scenes and isolated objects (Fig. 1C).

Selectivity for scenes and object properties

With our model of mid-level tuning for PPA in hand, we next sought to determine whether mid-level feature preferences in a feedforward model are sufficient to reproduce the multifaceted selectivity profile of the PPA for scenes, high-level object properties, and low-level contour statistics. We developed an approach that builds on a powerful two-fold procedure for characterizing cortical tuning profiles: first, highly parameterized encoding models are fit to neural data (as we have done with our mid-level tuning models), and second, *in silico* experiments are performed to reveal the interpretable, latent properties of these encoding models (23, 32–34). The strength of this two-fold procedure is that it combines the predictive power of highly parameterized models with the interpretability gained from *in silico* experiments. Here we developed an approach that leverages high-throughput experiments to rigorously assess the latent information content of our mid-level representations in the context of a large natural scene dataset. In doing so, we are able to address a critical challenge for studies of mid-level visual representation: namely, that mid-level features are notoriously difficult to describe in terms of their perceptual properties but may nonetheless correspond to interpretable directions along the natural image manifold (25, 35, 36).

We first sought to determine whether our mid-level model of the PPA exhibits a pattern of scene-selectivity in its mean activation to images of scenes, objects, and faces, which are the stimulus categories that are often used to localize the PPA. In the following analyses, we

refer to our mid-level encoding model of the PPA as simPPA (and we use a similar naming convention for other ROIs in the supplementary figures). We found that much like the actual PPA, the activations of our simPPA model to a set of localizer stimuli showed the typical pattern associated with scene-preferring areas, with response preferences ordered from scenes to objects to faces. In direct comparisons, the mean activation of simPPA was significantly greater for scenes relative to both objects ($t(702)=23.99$, $p=1e-96$) and faces ($t(702)=71.09$, $p=1e-100$) (Fig. 1C). It is worth noting that the scene-selectivity of simPPA is driven by mid-level feature tuning and cannot be attributed to spatial preferences, given that our encoding models involved a global max pooling procedure. Furthermore, although simPPA was trained to predict PPA responses to a diverse sample of natural scenes, it was never trained on the localizer stimuli examined here. Thus, these findings show that the mid-level feature tuning of simPPA is sufficient to generate a reliable pattern of scene-selectivity that generalizes to new stimuli.

We next sought to characterize the selectivity of simPPA for object properties. We were specifically interested in determining whether the mid-level feature preferences of simPPA are reliably associated with interpretable object properties in the statistics of natural scenes. To accomplish this, we developed a computational method to characterize how the activations of an image-computable encoding model are affected by the presence of specific object categories in the context of natural scenes, and we used behavioral studies to relate these findings to human-interpretable object properties. This approach, which we refer to as semantic-preference mapping, has several strengths. First, it allows us to determine how the seemingly ineffable mid-level features of simPPA are related to the nameable components of scenes (i.e., objects). Second, it allows us to determine how simPPA responds to objects in their natural image contexts. And third, it is scalable to a large sample of images (i.e., 10^4), allowing us to characterize the association between mid-level features and interpretable object properties in a manner that is broadly representative of natural scene statistics.

Semantic-preference mapping works by systematically occluding instances of objects from target categories in a large set of images and then assessing how model activations are affected by the occlusion of these objects (Fig. 1D). We used the ADE20K dataset of densely annotated scenes to perform targeted occlusions of objects from specific semantic categories. The ADE20K dataset contains 27,574 images of real-world scenes from a diverse array of scene categories (37). The objects in each image of this dataset have been manually segmented and labeled by an expert human annotator. We examined 85 categories of objects that each had at least 500 instances in the ADE20K dataset (these categories are listed in Supplementary Table 1). We performed targeted occlusions of all instances of these object categories and passed the occluded images to our encoding model (see Methods for details). For all units in the encoding model, we calculated the difference in activation for each occluded image relative to its corresponding original image, and we then calculated

the mean of this difference score across all instances of an object category. The resulting metric indicates how strongly the responses of the encoding model are affected by the presence of a target object category in an image (Fig. 1E). We refer to this metric as a selectivity index. As an illustrative example, if a unit in the encoding model hypothetically responded to the features of cars, then its responses would decrease whenever cars were occluded, and it would have a high selectivity index for the target category *car*. Note that we partialled out occluder size from the selectivity indices to ensure that our results could not simply be attributed to differences in occluder size across categories (see Methods for details). We also performed several experiments that verified the robustness of the semantic-preference mapping results to variations in occluder shape (i.e., oval vs. rectangle) and CNN initialization parameters (see Methods and Supplementary Fig. 3).

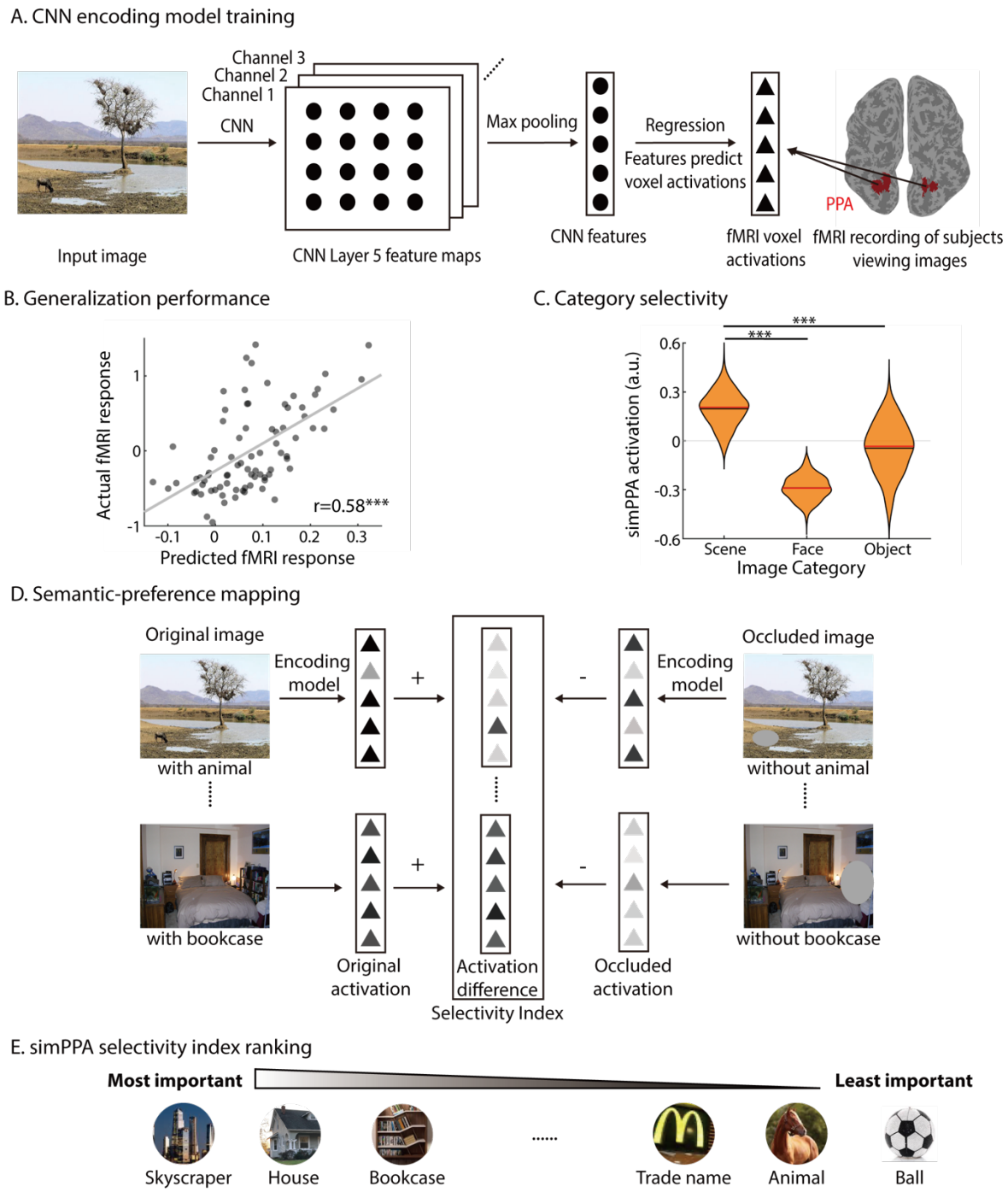

Figure 1. Encoding models and semantic preference mapping. A) Image-computable voxelwise encoding models of mid-level feature tuning were trained using the BOLD5000 fMRI dataset and the convolutional layers of a pretrained AlexNet CNN. The encoding models were created by truncating AlexNet at layer 5, adding a global max pooling operation, and then training a linear regression layer to map CNN feature activations to image-evoked fMRI responses. **B)** A strong test of generalization performance was conducted using data from Bonner & Epstein, 2021. The trained encoding models from BOLD5000 were used to generate predicted univariate fMRI responses in an ROI for a new set of stimuli and a new set of subjects. This plot shows the correlation between the predicted and actual fMRI responses in the PPA, which was strongly significant (r=0.58,

p=1e-5). **C)** Encoding model responses were obtained for a set of standard functional localizer images, including scenes, faces, and objects. The simPPA encoding model showed a preferential response to scenes relative to both faces and objects. Red and black lines indicate the median and mean of the distributions. **D)** In the semantic preference mapping procedure, a database containing densely segmented images is used to perform targeted occlusions of object categories and to assess how encoding model activations are affected by these object occlusions (37). This procedure is repeated for all instances of an object category in the database, and the results are averaged to produce the selectivity index for each object category. **E)** This panel illustrates the results of the semantic preference mapping procedure for simPPA by showing the object categories with the highest and lowest selectivity indices. ***p<0.001. CNN: Convolutional neural network. a.u.: arbitrary unit.

After calculating the selectivity indices for all 85 object categories, we then performed follow-up experiments to determine whether these selectivity indices were related to human-interpretable object properties. Specifically, we collected behavioral ratings for five properties that have previously been linked to the responses of the PPA: real-world size, fixedness, inanimate, manmade, and rectilinearity (13, 16, 18, 38) (Fig. 2A and Supplementary Figs. 4 and 5; see Methods for details). Because the manmade and inanimate ratings were highly correlated (r=0.91), we combined them into a single rating by taking their averaging for each category. We then calculated correlations of these object property ratings with the selectivity indices from our semantic-preference mapping procedure. For these correlations, we partialled out the size of the occluder for each object category to ensure that the correlations could not be attributed to occluder size (see Methods). We first calculated correlations with the mean selectivity index across all units in simPPA, which is analogous to examining the global univariate response of a brain region. We found that the mean selectivity index was significantly correlated with all four object properties, indicating that simPPA exhibits a preference for objects that are boxy, large in real-world size, fixed in location, and inanimate/manmade (Fig. 2B and Supplementary Fig. 6A). These results demonstrate that the known object preferences of the PPA, even for seemingly high-level properties like real-world size and fixedness, can emerge from purely feedforward computations of mid-level visual features and that these effects are representative of the statistical regularities in a large and diverse sample of natural scenes.

We next performed variance partitioning analyses to determine the degree to which our object-property ratings accounted for unique and shared variance in the selectivity of simPPA (see Methods for details). Rectilinearity had the highest correlation with the mean selectivity of simPPA (Fig. 2B), and our variance partitioning analyses showed that it could account for at least a portion of the explained variance associated with all three other object properties (Fig. 2C). For fixedness, the explained variance could be fully accounted for by rectilinearity. However, both real-world size and manmade/inanimate had unique

explained variance that could not be attributed to rectilinearity or any other property (Fig. 2C and Supplementary Fig. 6B). Thus, the mean response of simPPA exhibits preferences for the object properties of rectilinearity, real-world size, and manmade/inanimate that cannot be fully reduced to a common underlying factor.

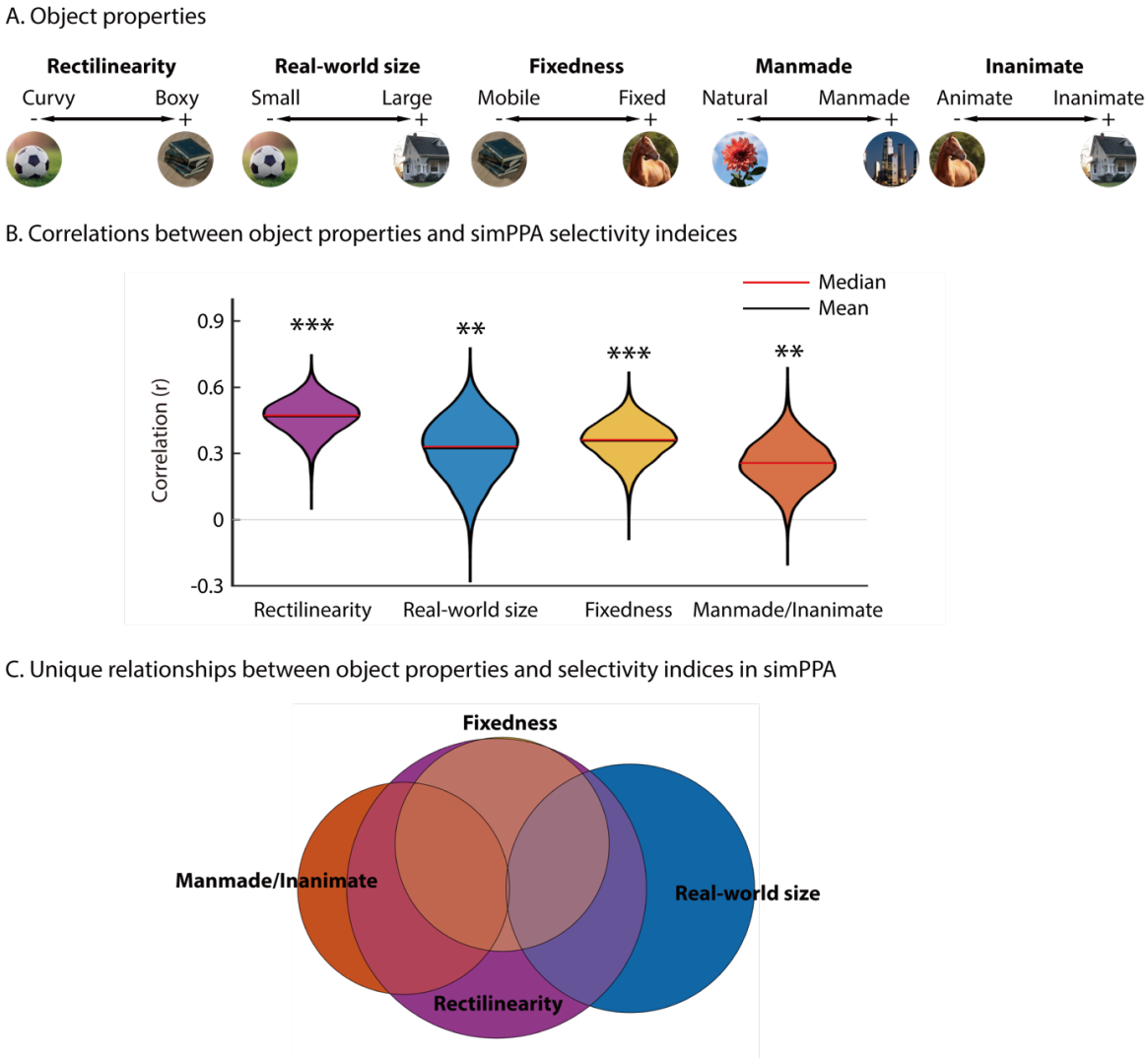

Figure 2. Univariate selectivity indices are correlated with interpretable object properties. A) Behavioral ratings were collected for object properties that have previously been associated with the responses of the PPA: rectilinearity, real-world size, fixedness, manmade, and inanimate. These ratings were collected for all 85 object categories that were examined in the semantic preference mapping procedure. Because manmade and inanimate were highly correlated, they were combined into a single manmade/inanimate rating. **B)** The average selectivity indices of simPPA were significantly correlated with all four object properties. This shows that the mid-level tuning of simPPA gives rise to preferential responses to objects that are rectilinear, large in real-world size, fixed in location, and inanimate/manmade. The violin plots show distributions of the correlation values across 10,000 bootstrap resampling iterations. **C)** Variance partitioning was used to identify the unique and shared contributions of each object property for explaining variance in the

selectivity indices of simPPA. There was a considerable amount of shared variance across the object properties. However, all properties other than fixedness also explained some portion of unique variance. See Supplementary Figure 6 for statistical assessments of the unique variance associated with each object property. *p<0.05, ***p<0.001. p-value calculated by permutation test (N=10,000).

Our analyses thus far have focused on the overall mean selectivity of simPPA. However, it is possible that these selectivity indices contain multiple latent dimensions of object preferences. We next performed analyses to examine the multivariate selectivity profile of simPPA and its principal representational dimensions. We applied principal component analysis (PCA) to the selectivity indices of simPPA for all 85 object categories from the semantic-preference mapping procedure. We focused on the first two principal components (PCs), which accounted for 82% and 7% of the variance in the selectivity indices. We then analyzed these PCs in the same way as the mean selectivity index. The first PC largely resembled the mean selectivity index, with significant correlations with all four object properties and unique explained variance for every property except fixedness (Fig. 3 and Supplementary Fig. 7A). Though the second PC accounted for far less variance than the first PC, it exhibited an interesting pattern of selectivity for large, natural/animate objects, with significant but opposite-signed correlations for real-world size and manmade/inanimate, which both explained unique variance (Fig. 3 and Supplementary Fig. 7A). Furthermore, there was almost no correlation with rectilinearity in the second PC. The results of these PC analyses show that when the multivariate selectivity of simPPA is broken down into its principal latent dimensions, we find two orthogonal patterns of selectivity: one for objects that are large and manmade and another for objects that are large and natural.

A. Correlations between object properties and PCs of selectivity indices in simPPA

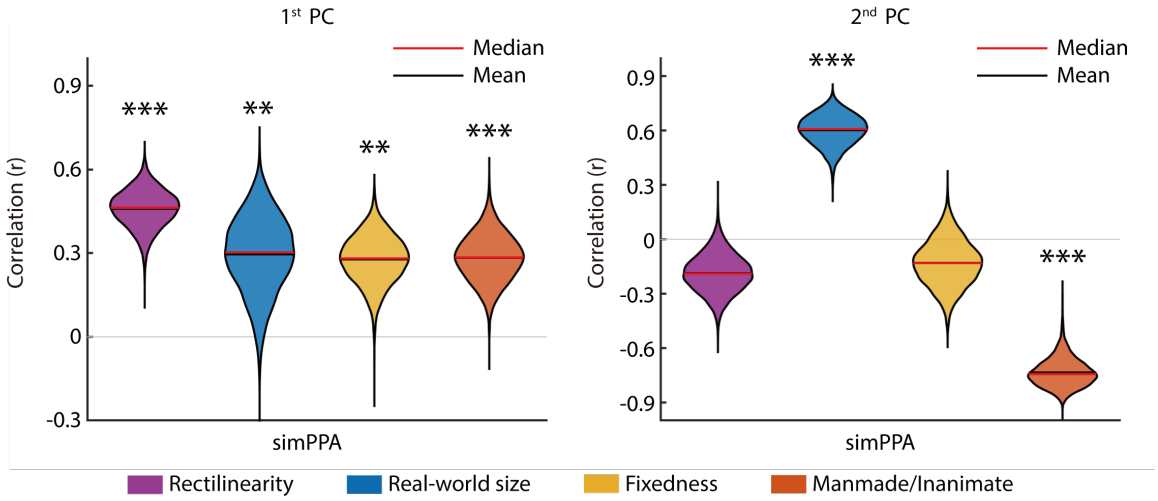

B. Unique relationships between object properties and PCs of selecitivity indices

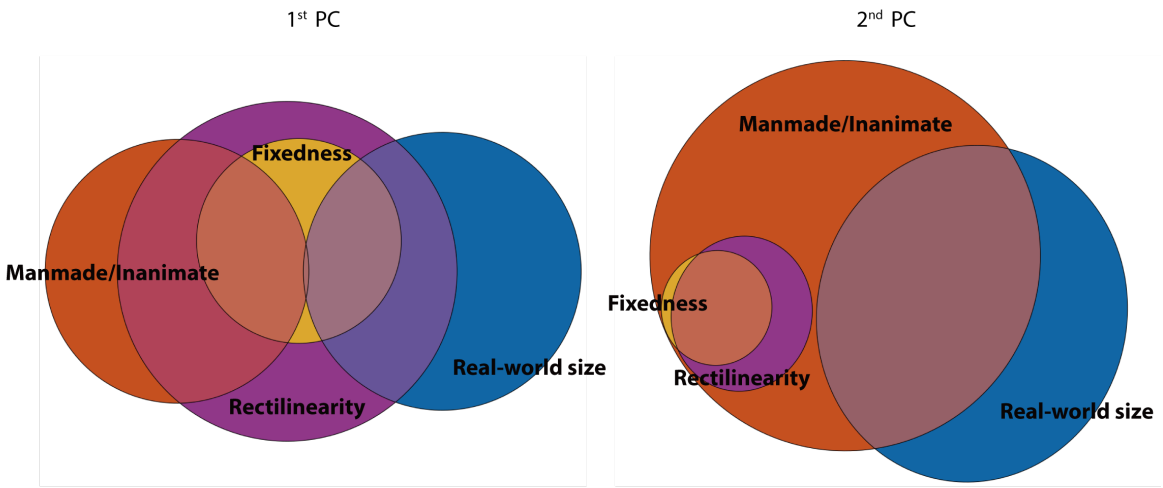

Figure 3. Principal components of the selectivity indices are correlated with interpretable object properties. A) As shown on the left, the first PC of the selectivity indices from simPPA was significantly correlated with all four object properties and resembled the findings for the global univariate selectivity indices. As shown on the right, the second PC of the selectivity indices exhibited a different pattern. This PC had significant but opposite-signed correlations with real-world size and manmade/inanimate and appears to reflect a preference for large, natural objects. The violin plots show distributions of the correlation values across 10,000 bootstrap resampling iterations. **C)** Variance partitioning was used to identify the unique and shared contributions of each object property for explaining variance in the selectivity indices of simPPA. For both PCs, there was a considerable amount of shared variance across the object properties. For the first PC, there are unique contributions from all properties other than fixedness. For the second PC, only inanimate/manmade and real-world size had unique contributions. See Supplementary Fig. 7 for statistical assessments of the unique variance associated with each object property. *p<0.05,

**p<0.01, ***p<0.001. p-value calculated by permutation test (N=10,000). PC: Principal component.

Selectivity for cardinal orientations and rectilinear shapes

One of the most perplexing aspects of the PPA is that in addition to its selectivity for scenes and high-level object properties, it also exhibits preferential responses to low-level geometric stimuli with a high proportion of rectilinear shapes and cardinal orientations (17–19). Here we tested whether our simPPA model of mid-level feature tuning also exhibits a similar pattern of response preferences for simple geometric stimuli. We created two sets of simple low-level stimuli to examine the response profile of simPPA across contour orientations and degrees of rectilinearity. We first examined simPPA responses to minimal images containing a single Gabor patch at a specific orientation, ranging from 0 to 165 degrees in 15-degree intervals (Fig. 4A). We found that, as in previous reports of the PPA, simPPA shows a response preference for contours at cardinal orientations (i.e., vertical and horizontal). An analysis of other ROIs showed that this preference for cardinal orientations was not a universal phenomenon of our encoding models but, instead, appeared to be specific to the scene-selective ROIs (Supplementary Fig. 8). We next examined simPPA responses to minimal images containing simple shapes that varied along a continuum from curvilinear to rectilinear (Fig. 4B). Again, much like previous reports of the PPA, simPPA showed a response preference to simple geometric stimuli with rectilinear features. This preference for rectilinear features was not a universal phenomenon of our encoding models but, instead, appeared to be specific to the scene-selective ROIs (Supplementary Fig. 9). Together, these findings show that the feedforward computation of mid-level visual features in simPPA gives rise to a multifaceted selectivity profile for scenes and object properties in natural images as well as for low-level contour statistics in minimal stimuli.

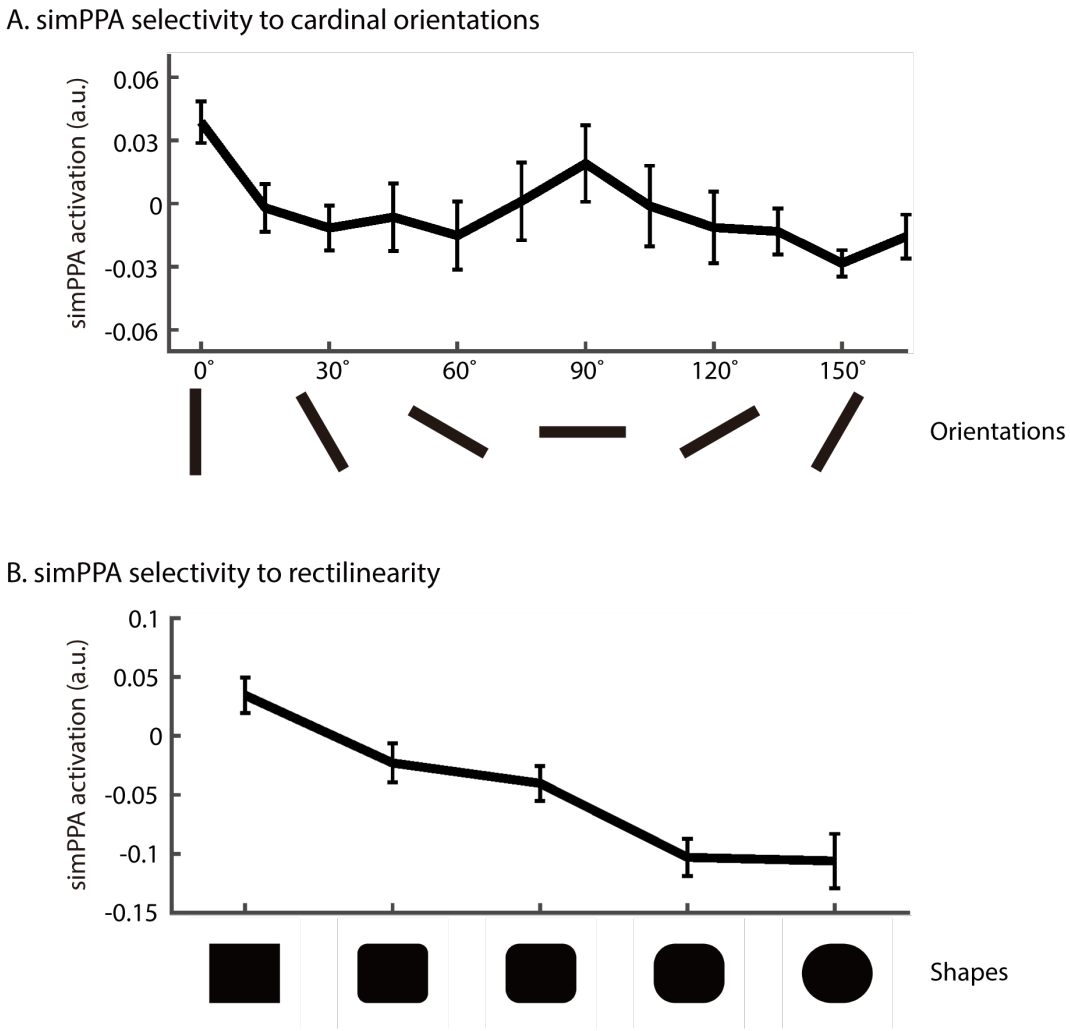

Figure 4. Selectivity for cardinal orientations and rectilinear shapes. The selectivity of simPPA for low-level perceptual properties was assessed using minimal stimuli containing oriented Gabor patches or simple shapes. **A)** The average univariate response of simPPA is plotted for stimuli containing Gabor patches at a range of angles from 0° to 165°. Error bars represent +/-1 SD across the units of simPPA. These findings show that simPPA responds more to contours at cardinal orientations (0° and 90°). **B)** The average univariate response of simPPA is plotted for stimuli containing simple shapes that varied along a continuum from boxy to curvy. Error bars represent +/-1 SD across the units of simPPA. These findings show that simPPA responds more to rectilinear shapes.

DISCUSSION

We fit a feedforward model of mid-level feature tuning to the scene-evoked fMRI responses of the PPA and found that it reproduced core aspects of PPA selectivity for scenes, object properties, and simple geometric stimuli. Using high-throughput, *in silico* experiments, we found that selectivity for interpretable image properties spanning from high-level conceptual attributes to low-level perceptual features can emerge from mid-level tuning

and natural image statistics. Our results provide a unified theoretical account of PPA selectivity that resolves several seemingly divergent findings on the response preferences of the PPA, and they show how the computational hierarchy of visual cortex can give rise to multifaceted selectivity profiles that span multiple levels of stimulus complexity.

Our results have implications for understanding the organizing principles of the ventral visual stream. One of the central anatomic properties of the ventral stream is its organization into patches that are selective for categories, such as places, faces, and objects, and coarse conceptual domains, such as those based on animacy and real-world size (38–40). Although this functional organization of the ventral stream has long been characterized in terms of high-level, interpretable stimulus attributes, such as categories, recent findings suggest that the fundamental organizing principles may be better characterized in terms of differential tuning to mid-level visual features (35, 36). One such finding showed that mid-level visual features are sufficient to elicit domain-selective fMRI activations in the ventral stream for the properties of animacy and real-world size, even when the experimental stimuli are unrecognizable as objects (36). Another key finding showed that the category-selective organization of object representations in the macaque ventral stream can be mapped onto the first two principal components of a feedforward CNN and may thus naturally arise from the statistical structure of mid-level feature representations (35). Moreover, multiple studies have shown that the representations of the human ventral stream are better explained by perceptual features than by the abstract properties that underlie category identity or human intuitions about semantic similarity (28, 28, 41–43). Our findings are broadly consistent with a mid-level theory of ventral-stream organization and show the surprising degree to which a feedforward model of mid-level feature tuning can account for the characteristic selectivity profile of the PPA for stimulus properties spanning from high-level, conceptual attributes to low-level contour statistics.

Although mid-level visual features are critical for explaining the cortical visual hierarchy, they are notoriously difficult to characterize (25). We lack simple algorithmic models of mid-level features, in contrast to the Gabor model for V1. The most effective approach for discovering mid-level visual features that are predictive of cortical responses is deep learning in CNNs (27, 44). However, the resulting CNNs are black boxes whose mid-level representations are challenging to visualize and even more challenging to describe in words—their features exist in an ineffable valley between the describable patterns of low-level vision (e.g., edges) and the intuitive concepts of visual semantics (e.g., objects). Here we sought to gain a more informative view of mid-level features by characterizing their covariance with nameable scene elements—a procedure we call semantic-preference mapping. This approach allowed us to combine the strengths of a CNN with the interpretability of a tuning profile across a set of object categories. Using this approach, we found that the mid-level features of our PPA encoding model had latent covariance relationships to interpretable object properties and that these covariance findings were

representative of the statistical regularities in the large and diverse sample of natural images examined here. These analyses provide a new perspective on PPA selectivity: they demonstrate that the strong responses of the PPA to scenes and landmark-like objects could in principle be mediated by the feedforward computation of mid-level features that covary with scenes and landmarks in the natural statistics of images.

It is important to point out that our findings do not simply reveal a confound between mid-level features and the high-level properties of scenes and landmarks. Rather, they reveal a potential mechanism for mediating the selectivity of the PPA during the passive viewing of natural images. After all, the PPA is a visual region that receives a large portion of its inputs from the visual pathway starting at the retina (26). Any mechanistic theory of the PPA will ultimately need to explain how it processes these downstream inputs in a manner that yields rapid and automatic selectivity for scenes and object properties. As an analogy, we could consider V1 cells, which are commonly described as being functionally selective for edges and are mechanistically modeled using oriented and localized spatial-frequency filters (45). The relationship between the mechanistic implementation (i.e., oriented spatial-frequency filters) and the functional selectivity (i.e., edges) is premised on the covariance between the filter responses and the presence of edges in images, but it does not require that this relationship be one of perfect mutual information. In fact, oriented spatial-frequency filters also provide information about image features other than edges and can even arise in models trained on spatially smooth images that contain no edges whatsoever (46). Despite this, there is little disagreement that V1 can be functionally described in terms of edge representation and that the underlying computational mechanisms involve spatial-frequency filters. Similarly, we argue that the PPA can be functionally described as representing scenes and landmark-like objects, and that one of the underlying mechanisms that directly supports this function is the feedforward computation of mid-level visual features.

It is also important to point out that our mid-level model does not capture all aspects of information processing in the PPA. Our model is only intended to account for the initial feedforward activations of the PPA and does not contain feedback and recurrent processes, which are pervasive in visual cortex and likely play a crucial role in the PPA. In fact, it is known that the PPA shows scene-related activation even without visual stimulation, including in subjects who are congenitally blind and in sighted subjects who are haptically exploring miniature scenes (21, 22). Thus, there appear to be scene-specific top-down feedback mechanisms in the PPA that remain to be explained. Our model is also spatially coarse and is focused on capturing tuning for mid-level features rather than spatial receptive-field biases. Although receptive-field biases are known to exist in the PPA (26), we found that our spatially coarse encoding model could nonetheless account for a substantial portion of the global univariate response profile of the PPA. Future work could examine how tuning to mid-level features interacts with the receptive-field biases of the PPA and to

determine whether there exist relevant covariance relationships between mid-level features and receptive-field locations in the natural statistics of vision (47). Our model is also not intended to explain the effects of navigational experience on the PPA, which shows stronger responses to objects that occur at navigationally important locations and treats stimuli as more similar if they come from the same place (14, 15, 48). Furthermore, our findings do not account for functional differences along the anterior-posterior extent of the PPA, which appear to reflect a general trend toward visual-form representations in the posterior PPA and mnemonic representations in the anterior PPA (31, 49, 50). However, future studies could leverage our mid-level modeling framework to test whether the effects of navigational experience in the PPA involve the modulation of mid-level features from navigationally important stimuli and to test whether the mnemonic representations of anterior PPA are implemented through the associative coding of mid-level features from co-occurring stimuli, including object categories in scenes and distinct views of places (14, 31).

Complex mid-level features may be the currency of the ventral visual stream (35, 36), and approaches for making sense of mid-level features are crucial for advancing our understanding of visual cortex. Here we show that when computational models of mid-level feature tuning in visual cortex are combined with methods for revealing their interpretable properties, these methods reveal how cortical selectivity profiles naturally span multiple levels of stimulus complexity and they provide insight into the category-selective organization of the ventral stream. More broadly, our computational modeling framework paves the way for examining the behavioral significance of mid-level features in scene- and landmark-processing and for exerting control over representational states in the cortical scene network through targeted visual stimulation (51, 52).

MATERIALS AND METHODS

fMRI data processing. We analysed data from the publicly available BOLD5000 dataset (https://bold5000.github.io), which contains 3T BOLD fMRI data in four subjects who viewed between 2,952 and 4,916 unique natural scene images depicting real-world environments and objects (29). This dataset was designed to sample fMRI activations to a large and diverse set of natural scenes. To maximize stimulus diversity, most images in this dataset were presented a single time over the course of the experiment. Stimuli were presented for 1 sec followed by a 9 sec interstimulus interval. In the scanner, subjects performed a valence judgment task, responding with how much they liked the image using the metric: "like", "neutral", "dislike". See (29) for a more detailed description of this dataset.

All functional data were preprocessed using fMRIPrep (53), which performed 3D motion correction, distortion correction, and co-registration to the T1 anatomical image. After preprocessing, we estimated the activation to each image using a series of general linear models that included a single regressor for each trial and another regressor for all other trials. This procedure has been shown to be more accurate for estimating activation magnitudes in event-related designs with high signal to noise (54). We implemented this general linear modeling procedure using the function 3DLSS in AFNI (55). These activation estimates were used as the predictands for our CNN encoding models.

ROIs were identified using four localizer runs. First, a group-based parcel derived from a large number of subjects was warped to each subject's native space to act as an anatomical constraint (56). Bilateral ROIs were identified within the parcel in each hemisphere by identifying the top 200 most activated voxels from the localizer contrast. PPA, OPA and RSC were identified using the scenes > objects contrast, LOC was identified using the objects > scenes contrast, and EVC was identified using the objects > scrambled contrast. In total, each subject had 400 voxels in each ROI.

Encoding models. We constructed voxelwise encoding models on top of the last convolutional layer of an AlexNet CNN that was pretrained on ImageNet (https://pytorch.org/hub/pytorch_vision_alexnet/). Our modelling procedure involved pooling and reweighting of the CNN responses from layer 5 (after ReLU) to predict the image activation estimates from BOLD5000 (Fig. 1A). We applied global max pooling to obtain a single activation for each feature channel in layer 5, and we passed these feature activations to a linear regression layer that was trained to predict the image-evoked fMRI activations as a weighted sum of the CNN feature activations. We trained the linear regression layer using LASSO (L1 penalized) regularization. A 10-fold cross validation procedure was used to search for the optimal regularization penalty in each voxel. The penalty parameter was selected from 20 values on a log-scale from 1e-4 to 1e4. After identifying the optimal penalty parameter for each voxel, we learned a set of regression

weights using this penalty parameter and the full set of fMRI data. Together, the truncated CNN (up to layer 5), followed by max pooling, and the regression layer define an image-computable encoding model of mid-level feature tuning for each voxel.

We were interested in L1 regularization as a means of learning sparse encoding models that emphasize the CNN features that are most important for each voxel. However, we were unsure if L1-regularized regression would perform as well as L2-regularized or ordinary least squares (OLS) regression. We therefore evaluated the performance of different regression methods by running encoding-model analyses on the BOLD5000 dataset with 10-fold cross-validation using OLS regression (without regularization), LASSO regression (L1 regularization) and ridge regression (L2 regularization). Although previous studies have typically used ridge regression when fitting voxelwise encoding models (32, 33), we found that LASSO outperformed both ridge and OLS (Supplementary Fig. 1, see Supplementary Fig. 10 for full OLS encoding model results). Thus, our encoding models benefited from a sparse regularization procedure that pushes some of the regression weights to zero and emphasizes the subset of feature activations that are most informative for each voxel.

Encoding model performance was evaluated in two ways. First, we performed a new 10-fold cross-validation procedure on the BOLD5000 dataset while keeping the regularization penalty fixed (using the previously learned optimal penalty for each voxel). The cross-validation scheme used for this evaluation was different from the cross-validation scheme that was used when selecting the regularization penalty. Supplementary Fig. 2A shows the mean Pearson correlations between the predicted activations and the observed activations across all cross-validation folds and all voxels in each ROI. Note that because the penalty parameter was learned on the same data, the performance estimates may be biased upwards. We therefore performed an additional stringent evaluation of encoding-model generalization performance using a separate set of fMRI data with new subjects and new stimuli, which is described below. It is also worth noting that the encoding models perform well above chance in the BOLD5000 dataset even when using OLS regression without regularization, which means that regularization is not required to achieve statistically significant performance (Supplementary Fig. 10). Furthermore, our results and conclusions do not depend on the specific values of the performance estimates in BOLD5000. It is already well-established that CNNs are state-of-the-art encoding models of fMRI responses in visual cortex (27). The primary goal of our analyses is to characterize the mid-level representations of these encoding models after they have been fit to fMRI data.

Second, to rigorously test generalization performance, we used the trained encoding models from the BOLD5000 dataset to predict the fMRI activations to 81 object categories from a separate fMRI dataset with a different set of subjects. We used the fMRI data from Bonner & Epstein, 2021 (https://osf.io/ug5zd/), which included fMRI responses in four subjects who viewed images of isolated real-world objects from 81 different categories that were

presented on meaningless textured backgrounds. In the scanner, the subjects performed a simple oddball-detection task of pressing a button whenever a warped object was shown. See the original publication for a detailed description of these data (31). Each object category in this dataset contained 10 unique images, which were shown in a block design. We ran all images through our CNN encoding models and obtained the average activation across all 10 images for each object category. Our goal was to test whether these encoding model activations could predict the average univariate fMRI activation of our ROIs. For each ROI, we averaged the encoding model activations across all voxels in all subjects from BOLD5000 to obtain a single activation value for each object category, which we compared with the actual univariate fMRI activations averaged over all subjects in the Bonner & Epstein data. We observed a strong correlation between the predicted activations from our encoding models and the actual fMRI activations in all ROIs (Supplementary Fig. 2B). These findings demonstrate that the encoding models trained on the BOLD5000 dataset exhibit remarkable generalization performance across both subjects and stimuli when predicting the univariate activations of multiple ROIs (including PPA). Thus, our encoding models appear to capture key aspects of the mid-level feature tuning in these ROIs.

Semantic preference mapping. We developed an algorithmic approach to examine how the activations of our CNN encoding models were affected by the object classes present in an image. For this procedure, we made use of the ADE20K dataset, which contains 27,574 images of real-world scenes from a diverse array of scene categories (37). The objects in each image of this dataset have been manually segmented and labeled by an expert human annotator. We used these segmentation masks to perform targeted occlusions of objects in images and assess how these occlusions affected the activation of the CNN encoding models (Fig. 1E). The logic of this procedure is that if an encoding model preferentially responds to certain categories of objects, then its responses will be strongly affected by occlusions of those objects. Our goal was to rigorously assess how the CNN encoding model activations were affected by the presence of these object categories in a large sample of images. We therefore examined all object categories that had at least 500 instances in the ADE20K dataset, which yielded a total of 85 categories (these are listed in Supplementary Table 1). For our targeted occlusions, we used the object segmentations to create the smallest oval mask that covered the target object. These masks contained random RGB values in each pixel, and the edges of these masks were blurred by morphological dilation using the Matlab function imdilate. We passed the occluded images to our CNN encoding models and calculated a difference score by subtracting the activation to the occluded image from the activation to the corresponding original images (without occlusion). We then calculated the mean of this difference score across all instances of an object category. The resulting metric indicates how strongly the responses of the encoding model are affected by the presence of a target object category in an image. We refer to this metric as a selectivity index. To ensure that our findings could not simply be attributed to the size of the occluders, we partialled out occluder size by regressing the selectivity indices against occluder size (i.e., mean

number of pixels) and retaining the residuals, which we used for all follow-up analyses. For univariate analyses of each ROI, we averaged the selectivity indices across all voxelwise models in all subjects. When performing PCA for each ROI, we concatenated the selectivity indices across all voxelwise models in all subjects.

We performed analyses to assess the robustness of the results obtained from the semantic preference mapping procedure. We first ensured that our findings were not contingent on the specific shape of the occluder (i.e., oval) by repeating our analyses using rectangular occluders. We found that the mean selectivity indices in each ROI were highly consistent whether we used oval occluders or rectangular occluders (Supplementary Fig. 3; all r-values >0.7, all p-values<0.0001). We next evaluated whether the results of the semantic preference mapping procedure were consistent when using CNNs with different random initializations during pretraining. To do this, we examined 10 different instances of AlexNet trained on the CIFAR dataset using different random initializations (57) (https://osf.io/3xupm/). We performed our entire pipeline of training encoding models and performing semantic preference mapping using these 10 different instances of AlexNet, and we compared the resulting selectivity indices across all 10 instances. We found that the mean selectivity indices in each ROI were highly consistent across all 10 instances of AlexNet (the mean pairwise correlations were greater than 0.9 for all ROIs).

Behavioral ratings of object properties. Fifty subjects were recruited online through the Prolific platform. This experiment was in compliance with procedures approved by the Johns Hopkins University Institutional Review Board. Subjects were asked to judge five object properties for a highlighted object in an image using a 7-point scale (Supplementary Fig. 4A). The judged object properties included curvature, real-world size, inanimate, manmade and fixedness. Each subject was presented with one image per each of the 85 object categories, with a total of 85 stimuli per subject. Stimuli were randomly chosen from the images used in the semantic preference mapping procedure. Subjects had the option of hovering a virtual magnifying glass over the image to enlarge any part of the image that was not clear. For each property, we used the average rating across all subjects in all follow-up analyses. As expected, some of these ratings covaried (Supplementary Fig. 5). We found that inanimate and manmade were highly correlated (r=0.91, p=1e-6), and we therefore decided to take the average of these two properties to create a combined manmade/inanimate rating.

Variance partitioning. We used variance partitioning to evaluate the degree to which the object-property ratings explained unique or overlapping variance in the selectivity indices. We performed these analyses using the vegan package in R (58). In these analyses, multiple object properties were used to predict the selectivity indices. Through a series of regressions using different subsets of object properties, we obtained the unique and shared variance associated with all object properties (see Figs. 2 and 3). We also separately performed simple partial correlation analyses to assess the unique contribution of each

object property after partialling out all other object properties from the selectivity indices (see Supplementary Figs. 6 and 7).

Analyses of contour orientations and rectilinear shapes. To test whether the encoding models preferred contours at specific orientations, we created minimal images with Gabor patches at different orientations, ranging from 0° to 165° in 15° intervals (see Fig. 4 and Supplementary Fig. 8). These images were 492-by-402 pixels in size and contained a single Gabor patch in the center that has a wavelength of 100 (100 pixels/cycle) with spatial frequency bandwidth of 1 and the spatial aspect ratio of 0.5. We also evaluated encoding model responses to minimal images containing simple geometric shapes. We created a series of stimuli that varied along a continuum from boxy to curvy (see Fig. 4 and Supplementary Fig. 9). These images were 720-by-720 pixels in size and contained a single shape in the center that spanned ~385 pixels in height and ~460 in width.

ACKNOWLEDGMENTS

We thank Alon Hafri and Emalie McMahon for comments on this manuscript. The data from Bonner & Epstein 2021 was funded by NIH grant R01EY022350.

REFERENCES

1. R. M. Cichy, Y. Chen, J.-D. Haynes, Encoding the identity and location of objects in human LOC. *NeuroImage* **54**, 2297–2307 (2011).

2. R. A. Epstein, C. I. Baker, Scene Perception in the Human Brain. *Annu. Rev. Vis. Sci.* **5**, 373–397 (2019).

3. K. Grill-Spector, Z. Kourtzi, N. Kanwisher, The lateral occipital complex and its role in object recognition. *Vision Res.* **41**, 1409–1422 (2001).

4. H. Hong, D. L. K. Yamins, N. J. Majaj, J. J. DiCarlo, Explicit information for category-orthogonal object properties increases along the ventral stream. *Nat. Neurosci.* **19**, 613–622 (2016).

5. S. Bracci, J. B. Ritchie, H. O. de Beeck, On the partnership between neural representations of object categories and visual features in the ventral visual pathway. *Neuropsychologia* **105**, 153–164 (2017).

6. I. I. A. Groen, E. H. Silson, C. I. Baker, Contributions of low- and high-level properties to neural processing of visual scenes in the human brain. *Philos. Trans. R. Soc. B Biol. Sci.* **372**, 20160102 (2017).

7. G. L. Malcolm, I. I. A. Groen, C. I. Baker, Making Sense of Real-World Scenes. *Trends Cogn. Sci.* **20**, 843–856 (2016).

8. H. P. Op de Beeck, J. Haushofer, N. G. Kanwisher, Interpreting fMRI data: maps, modules and dimensions. *Nat. Rev. Neurosci.* **9**, 123–135 (2008).

9. S. Thorat, D. Proklova, M. V. Peelen, The nature of the animacy organization in human ventral temporal cortex. *eLife* **8**, e47142 (2019).

10. R. Epstein, N. Kanwisher, A cortical representation of the local visual environment. *Nature* **392**, 598–601 (1998).

11. R. A. Epstein, Parahippocampal and retrosplenial contributions to human spatial navigation. *Trends Cogn. Sci.* **12**, 388–396 (2008).

12. R. A. Epstein, L. K. Vass, Neural systems for landmark-based wayfinding in humans. *Philos. Trans. R. Soc. B Biol. Sci.* **369**, 20120533 (2014).

13. J. B. Julian, J. Ryan, R. A. Epstein, Coding of Object Size and Object Category in Human Visual Cortex. *Cereb. Cortex* **27**, 3095–3109 (2017).

14. S. A. Marchette, L. K. Vass, J. Ryan, R. A. Epstein, Outside Looking In: Landmark Generalization in the Human Navigational System. *J. Neurosci.* **35**, 14896–14908 (2015).

15. L. Sun, S. M. Frank, R. A. Epstein, P. U. Tse, The parahippocampal place area and hippocampus encode the spatial significance of landmark objects. *NeuroImage* **236**, 118081 (2021).

16. V. Troiani, A. Stigliani, M. E. Smith, R. A. Epstein, Multiple Object Properties Drive Scene-Selective Regions. *Cereb. Cortex* **24**, 883–897 (2014).

17. P. B. Bryan, J. B. Julian, R. A. Epstein, Rectilinear Edge Selectivity Is Insufficient to Explain the Category Selectivity of the Parahippocampal Place Area. *Front. Hum. Neurosci.* **10** (2016).

18. S. Nasr, C. E. Echavarria, R. B. H. Tootell, Thinking Outside the Box: Rectilinear Shapes Selectively Activate Scene-Selective Cortex. *J. Neurosci.* **34**, 6721–6735 (2014).

19. S. Nasr, R. B. H. Tootell, A Cardinal Orientation Bias in Scene-Selective Visual Cortex. *J. Neurosci.* **32**, 14921–14926 (2012).

20. A. Schindler, A. Bartels, Visual high-level regions respond to high-level stimulus content in the absence of low-level confounds. *NeuroImage* **132**, 520–525 (2016).

21. T. Wolbers, R. L. Klatzky, J. M. Loomis, M. G. Wutte, N. A. Giudice, Modality-Independent Coding of Spatial Layout in the Human Brain. *Curr. Biol.* **21**, 984–989 (2011).

22. C. He, *et al.*, Selectivity for large nonmanipulable objects in scene-selective visual cortex does not require visual experience. *NeuroImage* **79**, 1–9 (2013).

23. M. F. Bonner, R. A. Epstein, Computational mechanisms underlying cortical responses to the affordance properties of visual scenes. *PLOS Comput. Biol.* **14**, e1006111 (2018).

24. S. Ullman, M. Vidal-Naquet, E. Sali, Visual features of intermediate complexity and their use in classification. *Nat. Neurosci.* **5**, 682–687 (2002).

25. J. W. Peirce, Understanding mid-level representations in visual processing. *J. Vis.* **15**, 5–5 (2015).

26. E. H. Silson, A. W.-Y. Chan, R. C. Reynolds, D. J. Kravitz, C. I. Baker, A Retinotopic Basis for the Division of High-Level Scene Processing between Lateral and Ventral Human Occipitotemporal Cortex. *J. Neurosci.* **35**, 11921–11935 (2015).

27. N. Kriegeskorte, Deep Neural Networks: A New Framework for Modeling Biological Vision and Brain Information Processing. *Annu. Rev. Vis. Sci.* **1**, 417–446 (2015).

28. I. I. Groen, *et al.*, Distinct contributions of functional and deep neural network features to representational similarity of scenes in human brain and behavior. *eLife* **7**, e32962 (2018).

29. N. Chang, *et al.*, BOLD5000, a public fMRI dataset while viewing 5000 visual images. *Sci. Data* **6**, 49 (2019).

30. A. Krizhevsky, One weird trick for parallelizing convolutional neural networks. *ArXiv14045997 Cs* (2014) (September 13, 2021).

31. M. F. Bonner, R. A. Epstein, Object representations in the human brain reflect the co-occurrence statistics of vision and language. *Nat. Commun.* **12**, 4081 (2021).

32. A. G. Huth, *et al.*, Decoding the Semantic Content of Natural Movies from Human Brain Activity. *Front. Syst. Neurosci.* **0** (2016).

33. M. D. Lescroart, J. L. Gallant, Human Scene-Selective Areas Represent 3D Configurations of Surfaces. *Neuron* **101**, 178-192.e7 (2019).

34. L. Tarhan, T. Konkle, Sociality and interaction envelope organize visual action representations. *Nat. Commun.* **11**, 3002 (2020).

35. P. Bao, L. She, M. McGill, D. Y. Tsao, A map of object space in primate inferotemporal cortex. *Nature* (2020) https:/doi.org/10.1038/s41586-020-2350-5 (June 4, 2020).

36. B. Long, C.-P. Yu, T. Konkle, Mid-level visual features underlie the high-level categorical organization of the ventral stream. *Proc. Natl. Acad. Sci.* **115**, E9015–E9024 (2018).

37. B. Zhou, *et al.*, Scene Parsing Through ADE20K Dataset in (2017), pp. 633–641.

38. T. Konkle, A. Oliva, A Real-World Size Organization of Object Responses in Occipitotemporal Cortex. *Neuron* **74**, 1114–1124 (2012).

39. N. Kanwisher, Functional specificity in the human brain: A window into the functional architecture of the mind. *Proc. Natl. Acad. Sci.* **107**, 11163–11170 (2010).

40. M. V. Peelen, P. E. Downing, Category selectivity in human visual cortex: Beyond visual object recognition. *Neuropsychologia* **105**, 177–183 (2017).

41. M. L. King, I. I. A. Groen, A. Steel, D. J. Kravitz, C. I. Baker, Similarity judgments and cortical visual responses reflect different properties of object and scene categories in naturalistic images. *NeuroImage* **197**, 368–382 (2019).

42. G. E. Rice, D. M. Watson, T. Hartley, T. J. Andrews, Low-Level Image Properties of Visual Objects Predict Patterns of Neural Response across Category-Selective Regions of the Ventral Visual Pathway. *J. Neurosci.* **34**, 8837–8844 (2014).

43. D. M. Watson, T. Hartley, T. J. Andrews, Patterns of response to visual scenes are linked to the low-level properties of the image. *NeuroImage* **99**, 402–410 (2014).

44. D. L. K. Yamins, J. J. DiCarlo, Using goal-driven deep learning models to understand sensory cortex. *Nat. Neurosci.* **19**, 356–365 (2016).

45. J. A. Mazer, W. E. Vinje, J. McDermott, P. H. Schiller, J. L. Gallant, Spatial frequency and orientation tuning dynamics in area V1. *Proc. Natl. Acad. Sci.* **99**, 1645–1650 (2002).

46. S. R. Lehky, T. J. Sejnowski, Network model of shape-from-shading: neural function arises from both receptive and projective fields. *Nature* **333**, 452–454 (1988).

47. D. Kaiser, G. L. Quek, R. M. Cichy, M. V. Peelen, Object Vision in a Structured World. *Trends Cogn. Sci.* **23**, 672–685 (2019).

48. G. Janzen, M. van Turennout, Selective neural representation of objects relevant for navigation. *Nat. Neurosci.* **7**, 673–677 (2004).

49. C. Baldassano, D. M. Beck, L. Fei-Fei, Differential connectivity within the Parahippocampal Place Area. *NeuroImage* **75**, 228–237 (2013).

50. E. H. Silson, *et al.*, A Posterior–Anterior Distinction between Scene Perception and Scene Construction in Human Medial Parietal Cortex. *J. Neurosci.* **39**, 705–717 (2019).

51. P. Bashivan, K. Kar, J. J. DiCarlo, Neural population control via deep image synthesis. *Science* **364** (2019).

52. C. R. Ponce, *et al.*, Evolving Images for Visual Neurons Using a Deep Generative Network Reveals Coding Principles and Neuronal Preferences. *Cell* **177**, 999-1009.e10 (2019).

53. O. Esteban, *et al.*, fMRIPrep: a robust preprocessing pipeline for functional MRI. *Nat. Methods* **16**, 111–116 (2019).

54. J. A. Mumford, B. O. Turner, F. G. Ashby, R. A. Poldrack, Deconvolving BOLD activation in event-related designs for multivoxel pattern classification analyses. *NeuroImage* **59**, 2636–2643 (2012).

55. R. W. Cox, AFNI: Software for Analysis and Visualization of Functional Magnetic Resonance Neuroimages. *Comput. Biomed. Res.* **3**, 162–173 (1996).

56. J. B. Julian, E. Fedorenko, J. Webster, N. Kanwisher, An algorithmic method for functionally defining regions of interest in the ventral visual pathway. *NeuroImage* **60**, 2357–2364 (2012).

57. J. Mehrer, C. J. Spoerer, N. Kriegeskorte, T. C. Kietzmann, "Individual differences among deep neural network models" (Neuroscience, 2020) https:/doi.org/10.1101/2020.01.08.898288 (November 21, 2020).

58. J. Oksanen, *et al.*, The vegan Package (2009).

SUPPLEMENTARY INFORMATION

Supplementary figures and tables for:

Tuning in scene-preferring cortex for mid-level visual features gives rise to selectivity across multiple levels of stimulus complexity

Shi Pui Donald Li and Michael F. Bonner

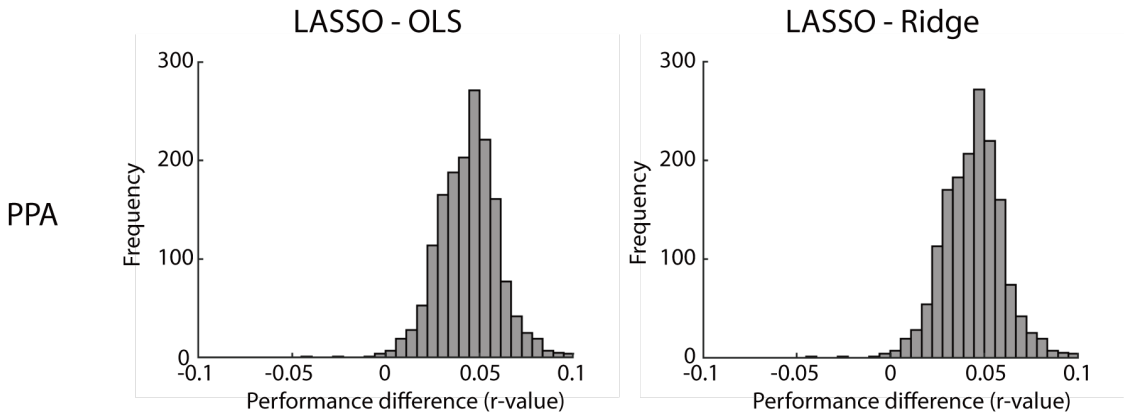

Supplementary Figure 1. Distribution of performance comparisons between regression methods. These plots show distributions of difference scores between the cross-validated prediction accuracies of voxelwise encoding models in the PPA that were trained using different regression methods. The difference scores were calculated by subtracting the prediction accuracy when using OLS (left panel) or ridge (right panel) from the prediction accuracy when using LASSO. These plots show that LASSO outperformed OLS and ridge in nearly all voxels. OLS: Ordinary least square. LASSO: Least absolute shrinkage and selection operator.

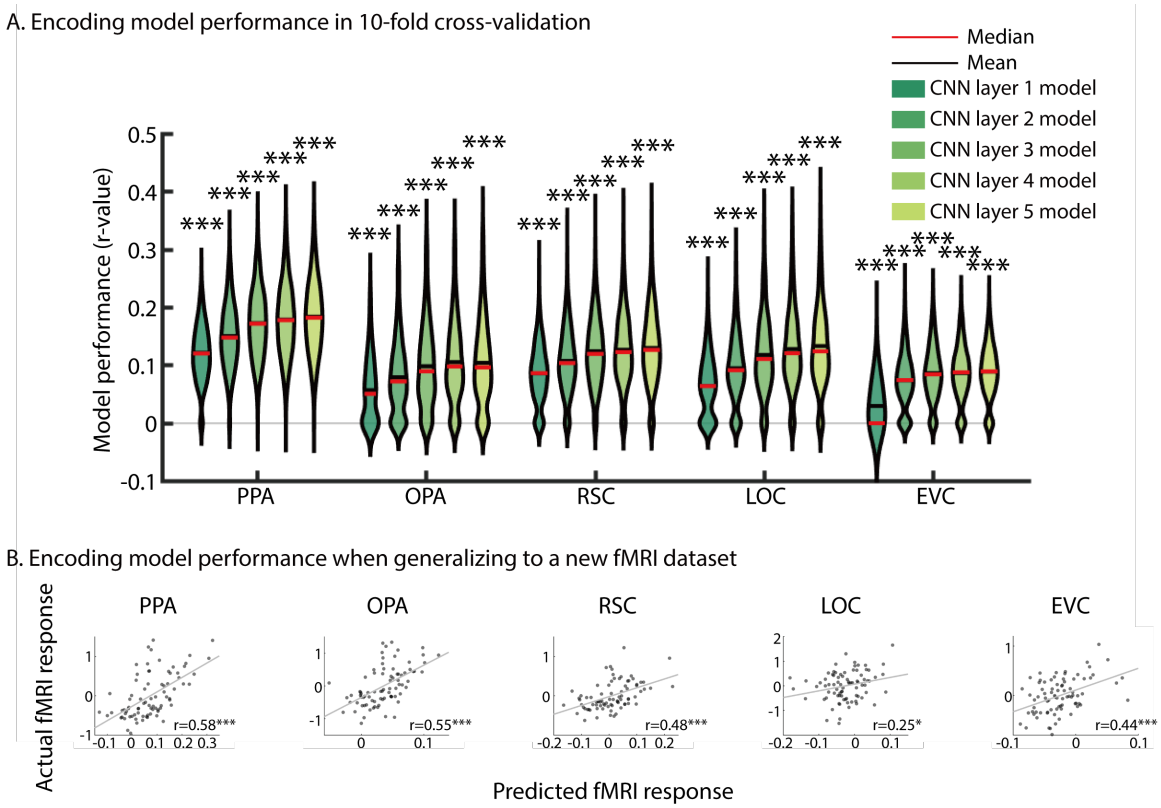

Supplementary Figure 2. Performance of CNN encoding models. A) Voxelwise encoding models were trained using each convolution layer of AlexNet followed by global max pooling and LASSO regression. Performance was assessed through 10-fold cross-validation on the BOLD5000 dataset. The average Pearson correlation of each voxel between the predicted and actual fMRI activations was computed across all folds of the cross-validation procedure. These violin plots show the distribution of encoding model performance across all voxels in all subjects for each ROI. **B)** A strong test of generalization performance was conducted by using the encoding models trained on BOLD5000 to predict the univariate activations of ROIs in a separate fMRI dataset with novel stimuli and different subjects. These analyses were performed using data from (31). Significant correlations between the predicted and actual fMRI responses were observed for all ROIs, showing that the encoding models trained on the BOLD5000 dataset exhibit strong generalization performance across both subjects and stimuli. *p<0.05, **p<0.01, ***p<0.001. p-value calculated by permutation test (N=10,000). CNN: Convolutional neural network.

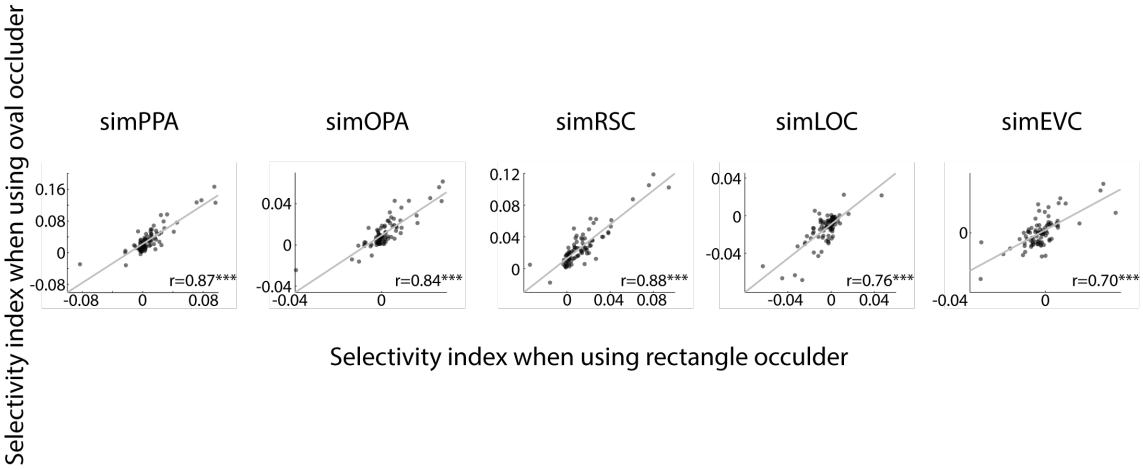

Supplementary Figure 3. Robustness of the semantic preference mapping results to variation in occluder shape. Semantic preference mapping was conducted using both oval and rectangular occluders. These scatter plots show that for each ROI, the average selectivity indices from semantic preference mapping were highly similar regardless of whether the occluders were ovals or rectangles. ***p<0.001. p-value calculated by permutation test (N=10,000).

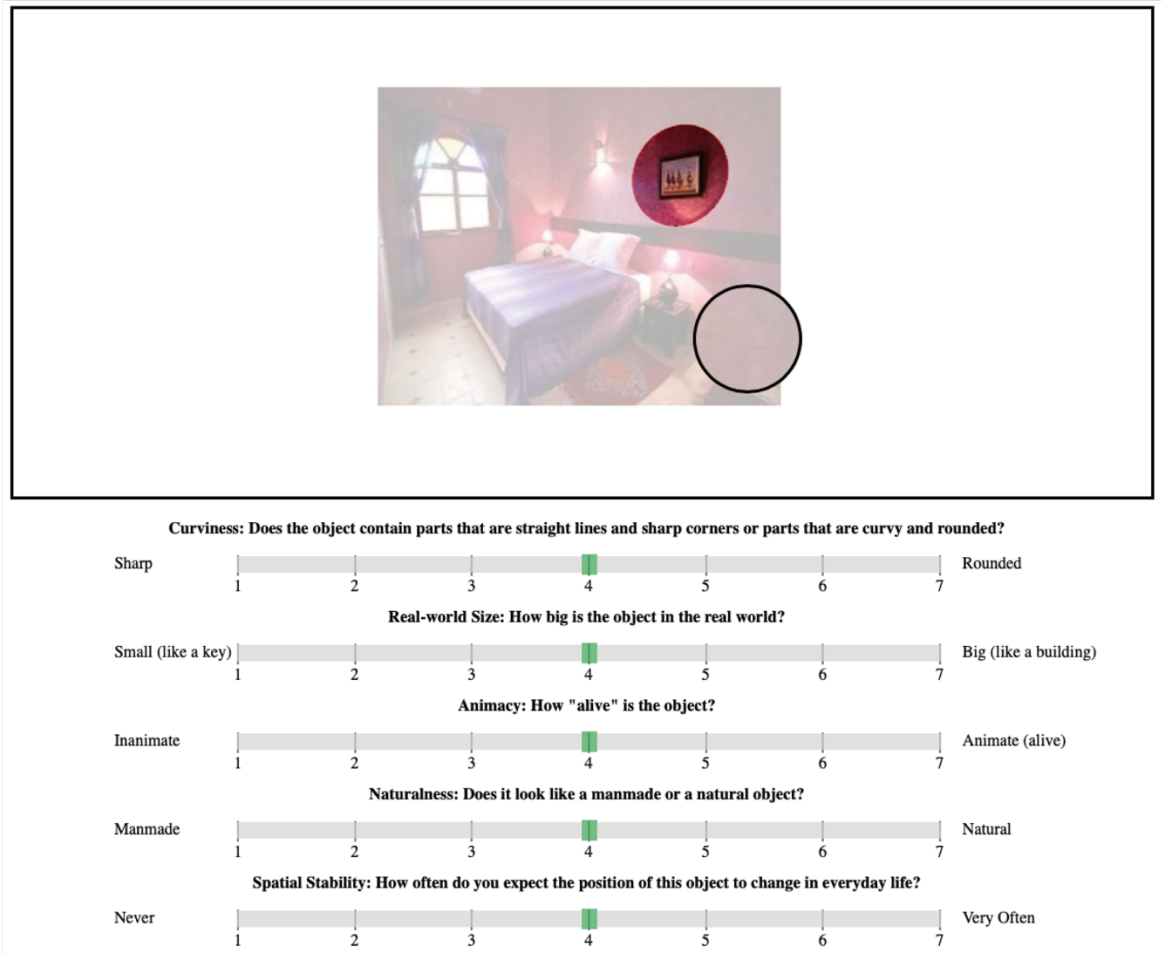

Supplementary Figure 4. Object property ratings. The image depicts the webpage interface from the object property rating experiments. The target object was highlighted with a red oval, and the rest of the image was faded. A virtual magnifying glass could be moved around to enlarge portions of the image. Subjects were asked to provide ratings using a slider for five properties of the highlighted object.

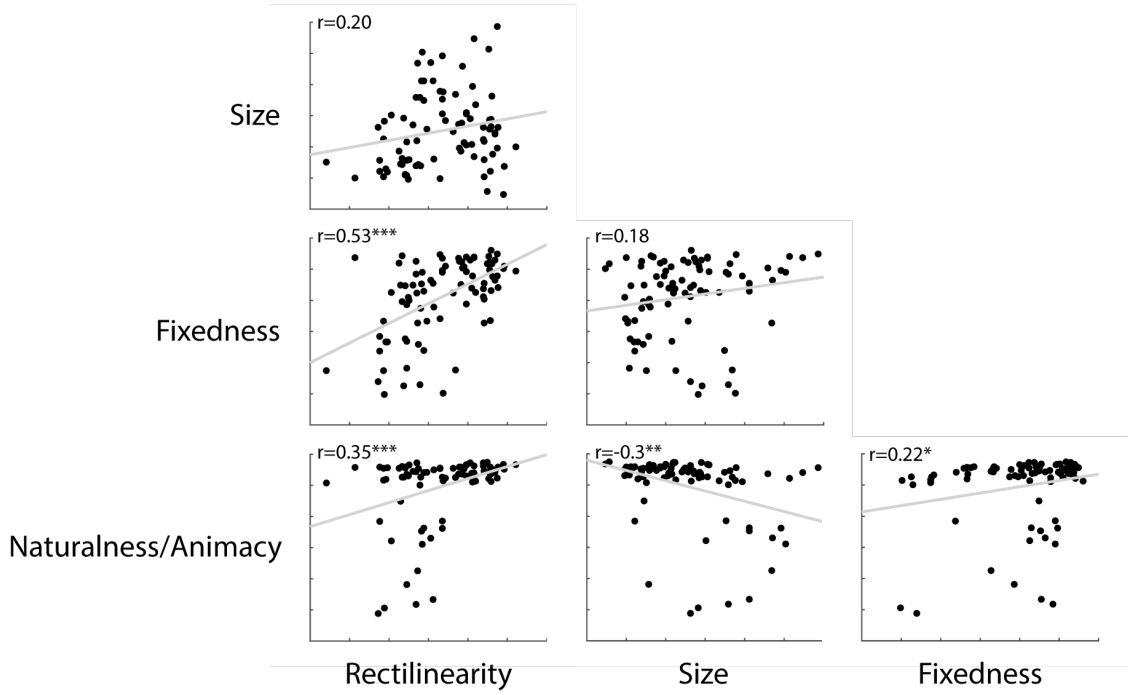

Supplementary Figure 5. Covariance of object property ratings. These scatter plot show all pairwise correlations between the object properties. *p<0.05, **p<0.01, ***p<0.001. p-value calculated by permutation test (N=10,000).

A. Correlations between object properties and selectivity indeices

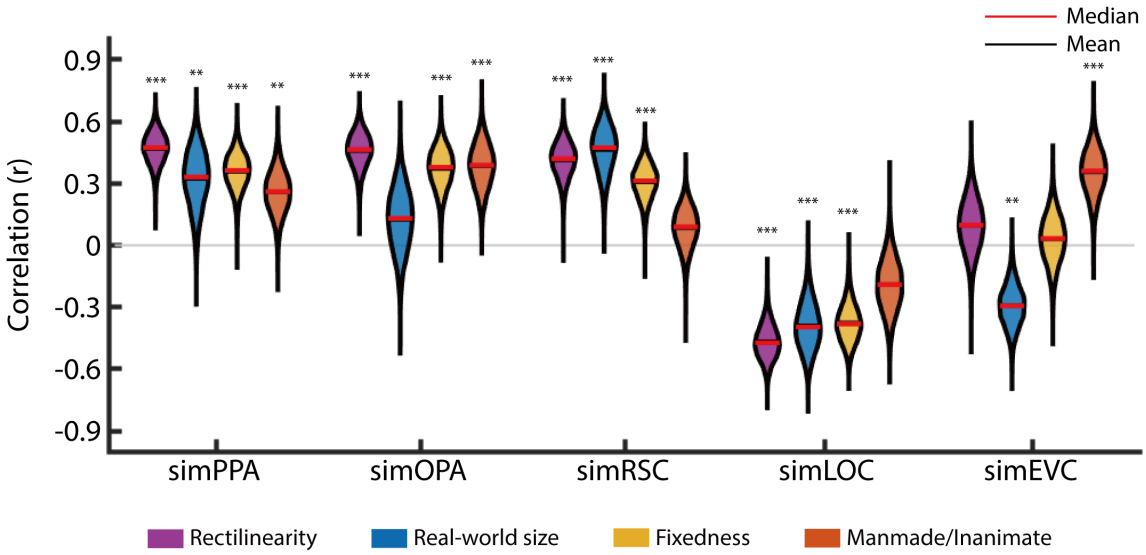

B. Unique relationships between object properties and selectivity indices

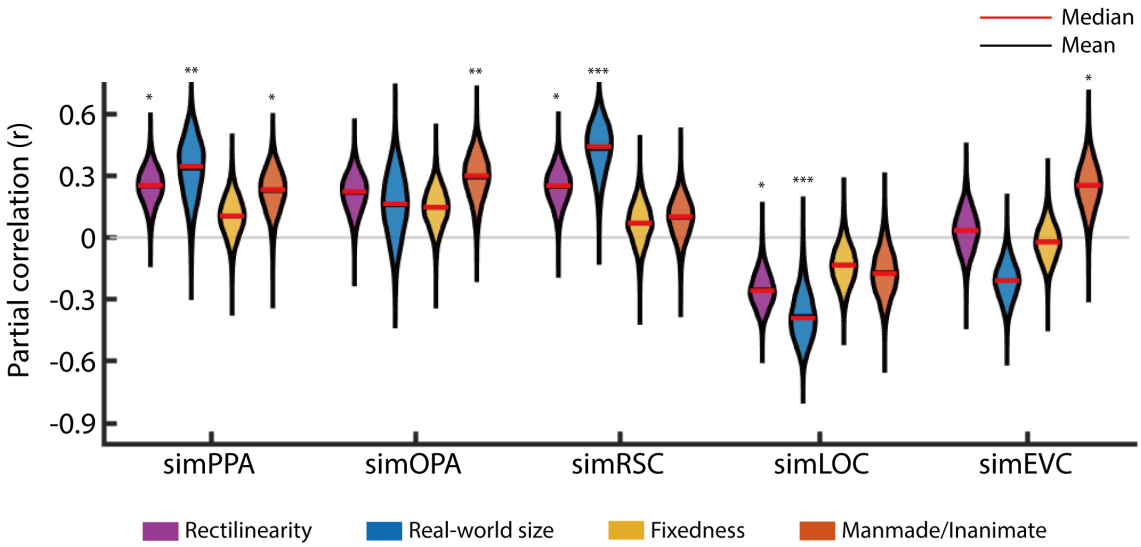

Supplementary Figure 6. Univariate selectivity indices are correlated with interpretable object properties. A) These plots show correlations between the average selectivity indices and the object properties in all ROIs. The violin plots show distributions of the correlation values across 10,000 bootstrap resampling iterations. **B)** Partial correlation analyses were performed to assess the unique contribution of each object property after partialling out all other object properties from the selectivity indices. *p<0.05, **p<0.01, ***p<0.001. p-value calculated by permutation test (N=10,000).

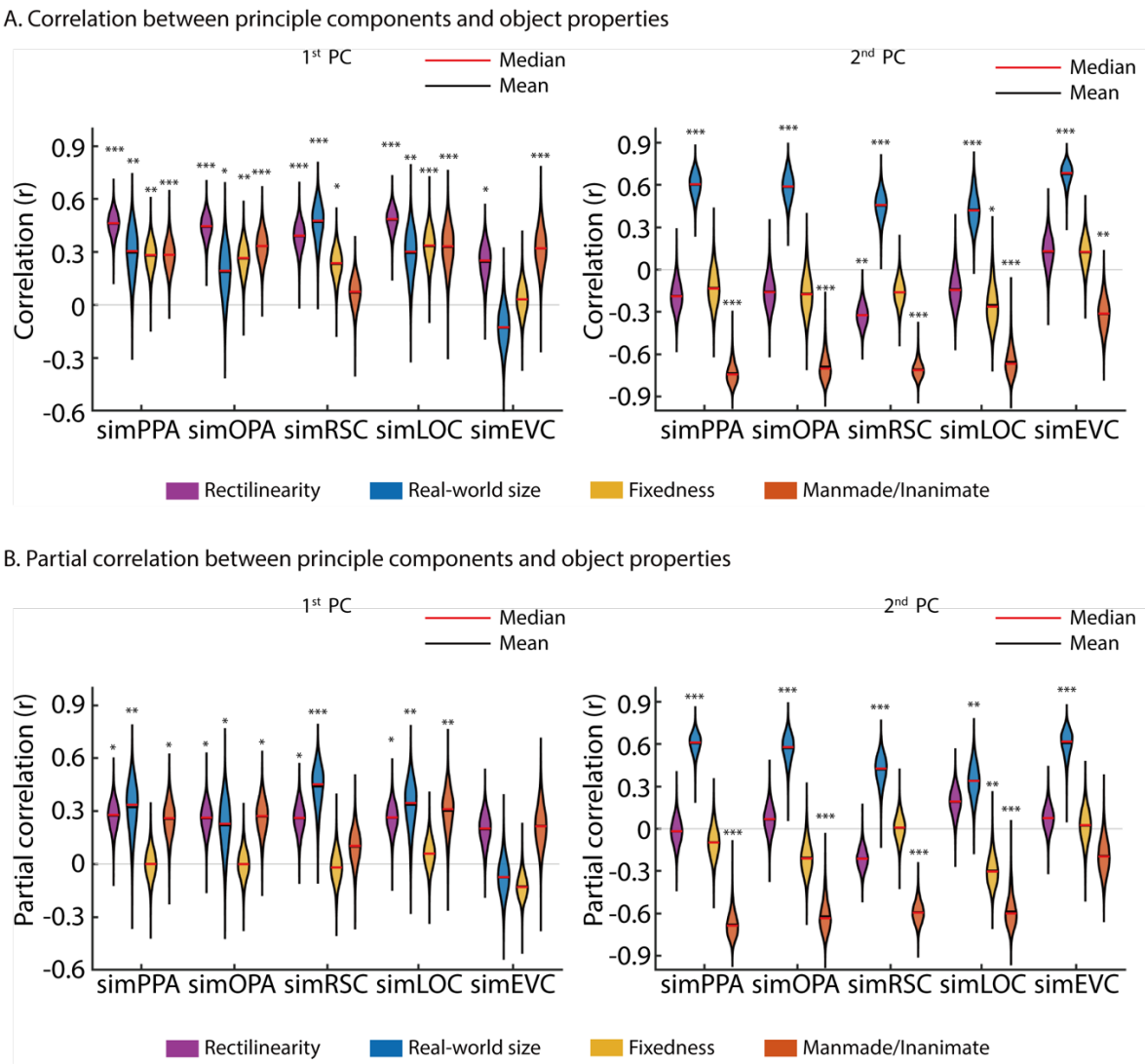

Supplementary Figure 7. Principal components of the selectivity indices are correlated with interpretable object properties. A) These plots show correlations between the PCs of the selectivity indices and the object properties in all ROIs. The violin plots show distributions of the correlation values across 10,000 bootstrap resampling iterations. **B)** Partial correlation analyses were performed to assess the unique contribution of each object property after partialling out all other object properties from the selectivity indices. *p<0.05, **p<0.01, ***p<0.001. p-value calculated by permutation test (N=10,000). PC: Principal component

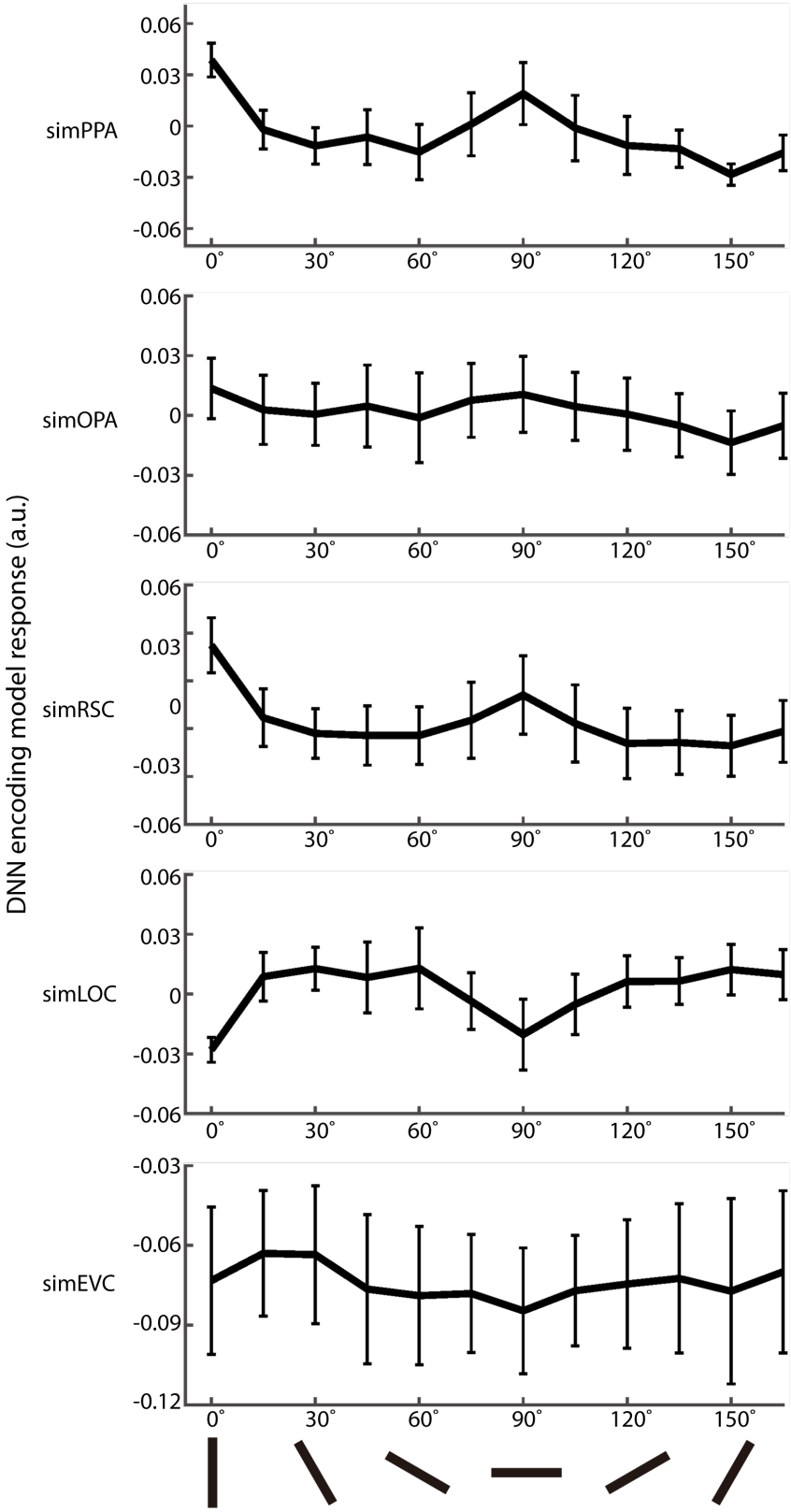

Supplementary Figure 8. Encoding models responses to contour orientations. The average univariate response of each ROI is plotted for stimuli containing Gabor patches at a range of angles from 0° to 165°. Error bars represent +/-1 SD across the units of each ROI.

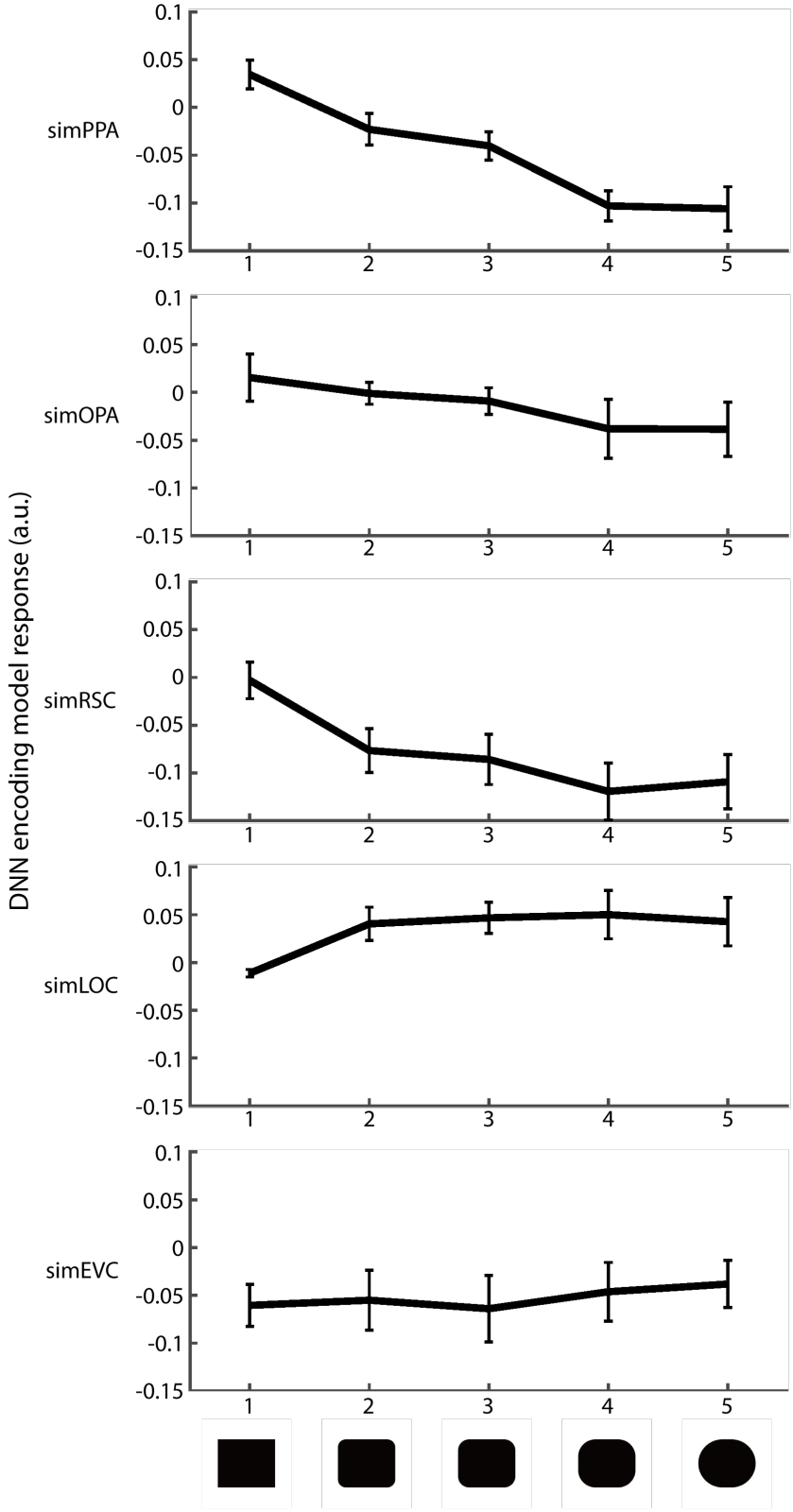

Supplementary Figure 9. Encoding models responses to simple shapes. The average univariate response of each ROI is plotted for stimuli containing simple shapes that varied along a continuum from boxy to curvy. Error bars represent +/-1 SD across the units of each ROI.

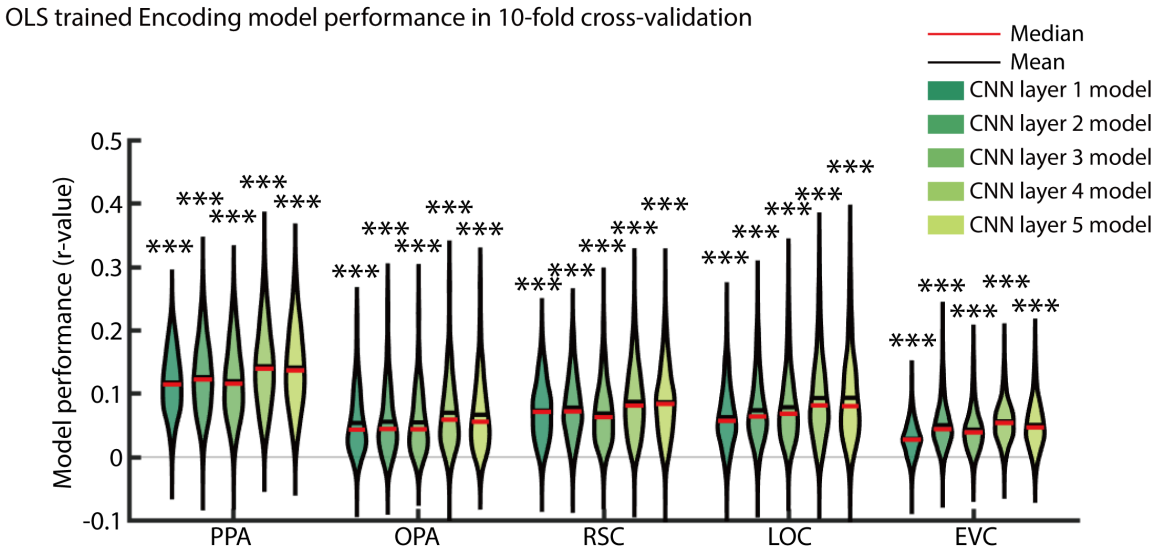

Supplementary Figure 10. Performance of CNN encoding models trained on ordinary least squares (OLS). Voxelwise encoding models were trained using each convolution layer of AlexNet followed by global max pooling and OLS regression. Performance was assessed through 10-fold cross-validation on the BOLD5000 dataset in the same way as the encoding models trained on LASSO regression in Supplementary Figure 2. *** indicates p<0.001

Supplementary Table 1. Object categories used for semantic preference mapping. This table shows all 85 object categories used in the semantic preference mapping procedure, with the objects sorted in descending order based on the selectivity indices for each ROI.

simPPA	simOPA	simRSC	simLOC	simEVC
building	skyscraper	building	animal	building
skyscraper	building	skyscraper	person	bookcase
house	bookcase	house	ball	food
bookcase	house	bookcase	towel	base
base	desk	base	stone	sofa
desk	base	road	pillow	fireplace
computer	computer	sky	shoe	ball
road	sofa	sea	flag	minibike
fireplace	fireplace	desk	figurine	car
floor	floor	field	glass	house
stove	stove	window	pot	desk
window	road	floor	bucket, pail	carpet
sofa	table	fireplace	telephone	bicycle
railing	coffee table	earth, ground	basket	road
sky	window	railing	wall socket	railing
dresser	carpet	sidewalk	fluorescent	table
table	food	computer	spotlight	sidewalk
carpet	dresser	grass	television	floor
coffee table	railing	stove	candlestick	coffee table
boat	boat	swivel chair	chandelier	computer
curtain	sink	sofa	electrical switch	armchair
sidewalk	armchair	boat	bicycle	truck
swivel chair	curtain	mountain	streetlight	toy
armchair	blind	path	sink	blind
column, pillar	book	fence	trash bin	book
painting, picture	sidewalk	dresser	stool	jar
food	swivel chair	table	light	boat
truck	monitor	carpet	air conditioner	plant
blind	television	coffee table	tin can	stove
sink	sky	curtain	minibike	traffic light
book	toy	armchair	swivel chair	electrical switch
fence	fence	column, pillar	poster	umbrella
monitor	column, pillar	car	magazine	wall socket
stairway	painting, picture	truck	toy	candlestick
bannister	truck	painting, picture	jar	sign
television	light	stairway	sign	magazine
sea	magazine	bush	monitor	trade name
toy	fluorescent	bannister	armchair	light
chandelier	jar	monitor	traffic light	glass
car	trash bin	book	umbrella	trash bin

stool	chandelier	sink	book	tin can
van	bannister	plant	palm tree	van
fluorescent	tin can	blind	stairs	air conditioner
magazine	stool	van	curtain	pot
earth, ground	stairway	chandelier	painting, picture	fence
poster	electrical switch	food	awning	dresser
light	candlestick	television	column, pillar	curtain
stairs	air conditioner	toy	trade name	streetlight
jar	basket	poster	bannister	figurine
plant	traffic light	palm tree	van	telephone
path	spotlight	stool	mountain	window
awning	stairs	stairs	plant	bannister
trash bin	wall socket	awning	stairway	awning
tin can	van	fluorescent	blind	stairs
sign	sign	magazine	bush	skyscraper
basket	bucket, pail	person	coffee table	spotlight
traffic light	pillow	tin can	table	palm tree
air conditioner	telephone	jar	truck	stool
candlestick	streetlight	basket	dresser	poster
bucket, pail	pot	light	car	basket
spotlight	figurine	traffic light	stove	fluorescent
umbrella	poster	sign	fence	television
streetlight	awning	umbrella	computer	monitor
electrical switch	plant	trade name	path	bucket, pail
telephone	path	trash bin	sofa	painting, picture
wall socket	sea	bucket, pail	boat	shoe
towel	umbrella	shoe	food	chandelier
pillow	towel	streetlight	carpet	flag
field	glass	towel	railing	earth, ground
trade name	bicycle	stone	window	pillow
pot	car	pillow	floor	stairway
figurine	earth, ground	air conditioner	fireplace	sink
grass	flag	spotlight	sidewalk	column, pillar
flag	trade name	candlestick	grass	grass
bicycle	shoe	flag	earth, ground	swivel chair
glass	minibike	figurine	desk	path
shoe	palm tree	telephone	sky	person
palm tree	mountain	electrical switch	field	field
minibike	field	minibike	sea	towel
bush	bush	pot	base	stone
mountain	grass	wall socket	skyscraper	bush
ball	ball	bicycle	road	mountain
stone	stone	glass	bookcase	animal
person	person	ball	house	sky
animal	animal	animal	building	sea